UNIVERSITY OF CALIFORNIA SAN DIEGO

Estimates of the direct radiative effect of Sonoran Desert dust from origin soil mineralogy - a multi-model study.

A thesis submitted in partial satisfaction of the requirements
for the degree Master of Science

in

Oceanography

by

Blake C. Walkowiak

Committee in charge:

Amato Evan, Chair
Robert Frouin
Nicholas Lutsko

2022

The Thesis of Blake C. Walkowiak is approved, and it is acceptable in quality and form for publication on microfilm and electronically.

University of California San Diego

2022

DEDICATION

I dedicate this thesis to everyone who has supported me during the making of this project. To my parents, grandparents, sister, and friends... thank you. You have provided me with everything required to succeed, and for that I am infinitely grateful.

I began this project with the hope of attaining knowledge that enables me to be a better steward of the planet. After many months of thought and research, my resolve to understand the natural world continues to be unwavering. I dedicate this thesis to the Earth.

TABLE OF CONTENTS

LIST OF FIGURES

LIST OF TABLES

ACKNOWLEDGEMENTS

I would like to acknowledge Professor Amato Evan for his support as the chair of my committee. From the first discussion to the final calculation, his guidance throughout this thesis was steadfast and is most appreciated.

I would also like to acknowledge Oliver Hoffman, Alexandra Kuwano, and Sophia Wynn for their contributions to the project.

Additionally, I would like to thank my Professors for sharing their immense knowledge and providing me the tools to engage in scientific inquiry. And my many peers for their comradeship and fruitful discussions on topics across the realm of Earth Science.

The scattering properties are obtained from the TAMUdust2020 database (https://zenodo.org/record/4711247). Radiation is modeled with the Rapid Radiative Transfer Model (RRTM; http://rtweb.aer.com/rrtm_frame.html).

ABSTRACT OF THE THESIS

Estimates of the direct radiative effect of Sonoran Desert dust from origin soil mineralogy - a multi-model study.

by

Blake C. Walkowiak

Master of Science in Oceanography

University of California San Diego, 2022

Professor Amato Evan, Chair

Mineral dust contributes significantly to the regional aerosol mass of the Sonoran Desert where wind-driven dust storms are commonplace. These suspended dust particles scatter and absorb solar and terrestrial radiation transmitted through the atmosphere. Here, we derive the source dependent optical properties of airborne dust in the arid regions adjacent to the Salton Sea. In effort to quantify the dust direct radiative effect, surface mineral abundance from the Airborne Visible/Infrared Imaging Spectrometer (AVIRIS) mission are utilized to derive bulk refractive indices ($N = n - ik$), extinction coefficients (β_{ext}), single scatter albedo (SSA), and asymmetry parameter (g) of airborne dust (size range 0.1 – 100 μm). Dust optical properties are input into

the Rapid Radiative Transfer Model (RRTM) to simulate dust influence on the atmosphere/Earth radiation budget. Following implementation of these optical properties, the model output is used to calculate atmospheric radiative fluxes (ΔF). Differences in dust iron content is found to be responsible for regional variability in k and SSA. Simulations of radiation at the surface, within the atmosphere, and top-of-atmosphere (TOA) reveal the dust shortwave and longwave direct radiative effect (DRE). Estimates of DRE at the TOA range from -26.5 to -5.59 Wm^{-2} among three emission sources, where greater iron content is associated with warming. Results indicate distinct radiative effects of bulk dust that is dependent on modeled mineral composition as a function of soil source mineralogy.

Introduction

Suspended mineral dust is a significant constituent of the Earth's atmosphere by mass and aerosol optical depth (Kok et al., 2017). Dust emission occurs across the World's arid regions where vegetation is sparse and strong surface winds are frequent. Once in the atmosphere, dust begins to influence the radiation budget of the Earth/atmosphere system by scattering or absorbing solar and infrared radiation (direct effect). Dust particles can influence water and ice cloud processes and cloud formation (indirect effect) under favorable atmospheric conditions (Mahowald and Kiehl, 2003). During periods of large dust storms the local and regional broad scale climate patterns can shift (changes in precipitation due to radiation perturbations), with highly variable emission events found annually across the globe (Goudie and Middleton, 1992; Li et al., 2004). Climate change and human land use can influence the mass of mineral dust in space and time with significant effects on aerosol radiative forcing, cloud microphysics, precipitation, human health, and ecological function (Rosenfeld et al., 2001; D'Odorico et al., 2013).

Compared to Greenhouse gases and other aerosol species, the dust direct radiative effect (DRE) remains highly uncertain (Myhre et al., 2013). The physical and chemical composition of dust particles are important for assessing the aerosol-radiation interactions. In regard to size, particles near the solar (shortwave) spectrum are considered scattering (cooling effect, negative DRE) for interaction with solar radiation. Those particle with sizes near terrestrial (longwave) wavelengths are considered absorbing (warming effect, positive DRE). The chemical composition of dust is less well known, particularly on smaller spatial scales (Balkanski et al., 2007; Claquin et al., 1999). Regional radiative forcing by Earth System Models (ESMs) have used the assumption of globally uniform dust properties (e.g., complex refractive indices, particle

shape, mixing state, and mineral composition), a major source of uncertainty. Recent work has focused on addressing these inaccuracies by describing the mineral composition of dust and assessing the sign and magnitude of the regional and global DRE (Scanza et al., 2015;Li and Sokolik, 2018). The minerals that make up a dust particle, unique to regional soil type, have different spectral absorption potential (e.g., iron oxides, quartz, clay) that is described by the imaginary part of the refractive index (Di Biagio et al., 2019). How and in what quantities different minerals make up dust particles and how the related properties impact the dust DRE is a motivating factor for this study.

Mineral maps have become available in the past two decades that quantify the mineral species of unique surface soil types. However, these samples are relatively minimal and the majority of semi-arid and arid regions do not have significant coverage (Journet et al., 2014). In effort to increase the accuracy of mineral soil composition measurements the Earth Surface Mineral Dust Source Investigation (EMIT) was commissioned by NASA (Green et al., 2020). As of the completion of this thesis the EMIT mission has begun placement of a Dyson imaging spectrometer on the International Space Station. The instrumentation will resolve the absorption bands of dust-forming minerals that will be processed into reflectance spectra and a final gridded surface map product of mineral composition for ESM initialization. Data used in this work was accessible from the Airborne Visible/Infrared Imaging Spectrometer (AVIRIS) mission, the on-planet testing and validation flights for EMIT.

Determined here is the mineral dust DRE over three suspected emission zones within the Salton Sea region as a first impact study of the proposed products from EMIT. Surface mineral composition data is obtained from AVIRIS flights over the region as the EMIT system has a grace period between ISS install and fully functional operation. Soil mineral fractions are first converted to dust aerosol fractions for calculation of a bulk dust refractive index. Next, optical properties of the mineral dust are modeled using an irregular particle shape database that employs light scattering computations. Dust optical properties and appropriate aeolian dust atmosphere meteorology is input into a radiative transfer model for final DRE calculation.

Findings suggest differences in the optical properties of intraregional dust emission is caused by the spatial variability of specific mineral fractions, namely the iron containing species hematite. Additionally, varying mineral content can affect the sign of the dust DRE (heating or cooling).

Chapter 1

Methods

In the following sections, the process of deriving the bulk dust aerosol complex refractive index (CRI) and modeling of dust/radiation interaction is described. Mineral fractions for source soils and the AVIRIS/EMIT aerial products are passed through these methods to simulate dust emission and investigate the DRE of the specified mineralogy.

1.1 Soil to Aerosol Mineralogy

Three regions west of the Salton Sea were chosen to represent important emission sources of regional dust. Figure 1.1 shows the Clark Lake, Exposed Playa, and West desert emission regions where soil mineral composition data was gathered from the AVIRIS web portal. The Clark Dry Lake bed is located in a ”pull-apart” basin (an area of low elevation from fault activity) that is arid most of the year (red shading, Figure 1.1). Exposed Playa is found surrounding the shoreline of the Salton Sea and continues to reveal sediment with increased water loss through evaporation (green shading, Figure 1.1). The West Desert region is located within the greater Anza Desert and hosts multiple dry stream beds filled with fine sediments (blue shading, Figure 1.1). The AVIRIS grid maps provide mineral aggregated spectral abundance fractions for 9 minerals - illite, kaolinite, montmorillionite, calite, gypsum, hematite, goethite, chlorite, and dolomite - along with the bare soil fraction, but does not provide information on quartz and feldspar (key absorbing species in the longwave).

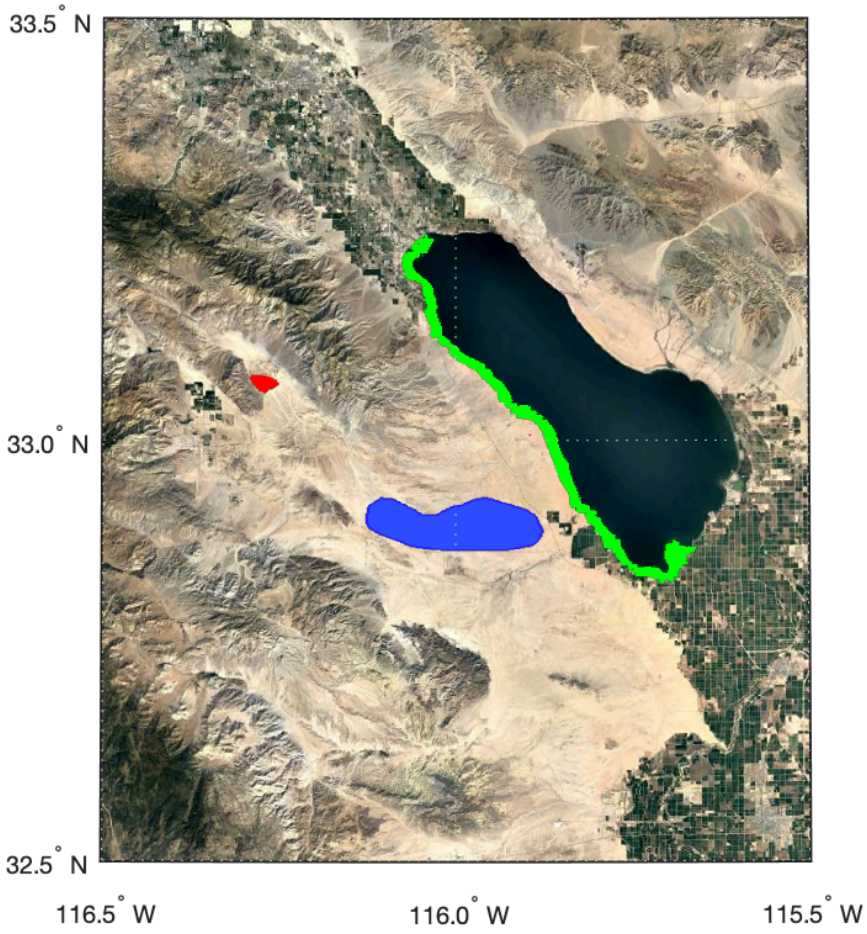

Figure 1.1. Satellite image of the Salton Sea with surrounding agricultural fields and desert. The Clark Lake, Exposed Playa, and West Desert emission regions are demarcated by the red, green, and blue shaded polygons, respectively.

Derivation of bulk aerosol refractive indices requires knowledge of the clay (0-0.2 μm) and silt (0.2-50 μm) mineral mass fractions specific to regional soil type (Scanza et al., 2015). The emitting soil types of the West Sonoran Desert are Luvic Yermosols (Yl) and Calcaric Fluvisols (Jc), the former is more expansive, encompassing the arid southwestern US, and the latter represents the desert playa and agricultural top soil adjacent to the Salton Sea (FAO/UNESCO Soil Map). Source soils and corresponding mineral information are obtained from the mean mineralogical table developed by Claquin et al. (1999) and mineral database from Journet et al.

Table 1.1. Soil mineral fractions specific to the Salton Sea region. Contains the clay and silt mass fractions of each mineral corresponding to the Yl and Jc soil types as documented in the mean mineralogical table developed by Claquin et al. (1999) and mineral database from Journet et al. (2014). The second half of the table hosts the AVIRIS surface mineral composition for the Clark Lake (CL), Exposed Playa (EP) and West Desert (WD) emission regions.

Soil type |	Clay fraction										Silt fraction									
	Ill	Kaol	Mont	Cal	Quar	Feld	Gyp	Hem	Chl	Dol	Ill	Kaol	Mont	Cal	Quar	Feld	Gyp	Hem	Chl	Dol
Jc	22	9	46	11	12	0	0	1	0.1	11	0	0	0	29	30	1	38	2	0.1	29
Yl	43	20	20	7	7	0	0	2	0	7	0	0	0	5	69	2	23	1	0.1	5
$Jc_{J,2014}$	42.8	9.7	7.9	25.2	2.7	0	0	2.4	7.9	25.2	18.2	0	0	29	36.4	1	18.2	0	9.1	29
$Yl_{J,2014}$	-	-	-	-	-	-	-	-	-	-	18.2	0	0	5	36.4	2	18.2	1	9.1	5

Region |	AVIRIS										
	Ill	Kaol	Mont	Cal	Quar	Feld	Gyp	Hem	Chl	Dol	Goe
CL	1.9	0.11	21.4	0.2	-	-	9e-3	8e-3	8.3e-4	0	0.06
EP	0.05	0.17	14.7	0.48	-	-	1.6	0.02	0.01	0.02	0.06
WD	0.42	2.9	2.4	7.3	-	-	4.9e-3	0.48	1.7e-3	2e-3	1.8

(2014) (Claquin et al., 1999; Journet et al., 2014). The mineral table contains data from sparse sampling studies with large extrapolations whereas the mineral database is incomplete for the clay fraction of the Yl soil type (Table 1.1). Soil mineral data and modified tables are aggregated to include the soil fractions of the 9 AVIRIS/EMIT minerals with the addition of quartz and feldspar. Missing quartz and feldspar fractions from AVIRIS in the clay and silt sizes are first assumed to follow the Jc soil fraction (clay: 30% feldspar, 70% quartz; silt: 56% feldspar, 44% quartz). A second partitioning of quartz and feldspar is modeled as an even split in the clay and silt (50% quartz; 50 % feldspar).

Dust emission originates from surface soils primarily by saltation, a mechanism where strong winds force sand sized particles (100-500 μm) to roll and bounce across the surface whereby smaller dust sized aggregates (diameter < 20 μm) are ejected and can have long-term suspension in the atmosphere (Gillette et al., 1974; Shao, 2001; Kok, 2011). Without this sandblasting dust size particles would not be emitted from the surface as cohesive forces of the soil particles counter the wind sheer. Modeled particle diameters extend to 100 μm to account for short-term suspension near the emission source. Here, wind driven dust emission is modeled following the Brittle Fragmentation Theory developed by Kok et al. (2011). Accordingly, dust

aerosol production consists of one or more particles combined in aggregates such that the aerosol size D_d is proportional to the volume fraction of origin soil particles with size $D_s \leq D_d$,

$$dN_d/dlnD_d \propto \int_0^{D_d} P_s(D_s)\, dD_s$$

where N_d is the normalized emitted particle number of dust aerosols with size D_d and P_s is the particle size distribution (PSD) of the soil. A log-normal expression is assumed to describe the fully disaggregated size distribution of soil particles (Kolmogorov, 1941),

$$P_s(D_s) = \frac{1}{(D_s\sqrt{2\pi}ln(\sigma_s)} * exp[-\frac{ln^2(D_s/\bar{D_s})}{2ln^2(\sigma_s)}]$$

where σ_s is the geometric standard deviation and $\bar{D_s}$ is the median diameter by volume. The "typical" dust PSD is defined by an average of multiple arid soil field measurements which indicate a uniform average $\bar{D_s} \approx 3.4\mu$m and $\sigma_s = 3.0$. The origin soil mineral clay and silt fractions that compose a given dust particle with size D_d are calculated by integrating over the entire PSD following equations 3a and 3b from Scanza et al. (2015),

$$f_{soil,clay} = \int_0^{D_{clay}} P_s(D_s)\, dD_s / \int_0^{D_d} P_s(D_s)\, dD_s$$

$$f_{soil,silt} = \int_{D_{clay}}^{D_d} P_s(D_s)\, dD_s / \int_0^{D_d} P_s(D_s)\, dD_s$$

where D_{clay} = 2 μm, $D_d > D_{clay}$, and f_{clay} and f_{silt} are the total clay and silt fractions which sum to unity. We note that these variables are sourced from limited measurements and a portion of the sampled PSDs were not fully dispersed. Specific chemical speciation within in PSD would enable a more robust calculation of the individual mineral fractions in the soil clay and silt sizes, rather than relying on the mineral maps comprised of relatively few measurements. Information about how the minerals in our region are segregated by size within the local soil PSD was not acquired for this thesis. Therefore, the information available from the soil maps is utilized for

calculating the individual mineral clay and silt fractions. The equation presented for the PSD is, however, used to derive the volume size distribution necessary in calculating the dust aerosol clay and silt fraction.

The mapped soil mineral clay and silt fractions are then used to generate mineral abundance weights calculated as follows:

$$w_{c,i} = f_{c,i}/f_{V,i}$$

$$w_{s,i} = f_{s,i}/f_{V,i}$$

where $f_{c,i}$ and $f_{s,i}$ are the individual mineral clay and silt fractions from the Jc soil (Table 1.1) and $f_{V,i}$ is the total soil fraction of each mineral. The Jc soil type is used due to the expansive surface coverage and complete mineral abundance values in both the clay and silt fractions. Retrieved surface mineral fractions from AVIRIS/EMIT (fE_i) are converted to soil clay and silt mass fraction weighted products using the weight individual fractions $w_{c,i}$ and $w_{s,i}$ for clay and silt, respectively.

$$fE_{c,i} = w_{c,i} * fE_i$$

$$fE_{s,i} = w_{s,i} * fE_i$$

where $fE_{c,i}$ and $fE_{s,i}$ represent the individual soil clay and silt particle fractions that constitute emitted dust aerosol with diameter D_d. The next step is to calculate the the aerosol fractions. In deriving the clay and silt aerosol fractions we first invoke equations 6a and 6b from Scanza et al. (2015) which combine equations 3a and 3b with the PSD,

$$fE_{clay}(D_d) = \frac{1 + erf[\frac{ln(D_{clay}/\bar{D_s}}{\sqrt{2}ln(\sigma_s)}]}{1 + erf[\frac{ln(D_d/\bar{D_s}}{\sqrt{2}ln(\sigma_s)}]}$$

$$fE_{silt}(D_d) = \frac{erf[\frac{ln(D_d/\bar{D}_s}{\sqrt{2}ln(\sigma_s)}] - erf[\frac{ln(D_{clay}/\bar{D}_s}{\sqrt{2}ln(\sigma_s)}]}{1 + erf[\frac{ln(D_d/\bar{D}_s}{\sqrt{2}ln(\sigma_s)}]}$$

where erf is the error function, $fE_{clay}(D_d)$ + $fE_{silt}(D_d)$ = 1 or, in other words, at each particle size there exists a clay fraction and a silt fraction, and $fE_{clay} \geq 1$ and $fE_{silt} \leq 0$ when $D_d < D_{clay}$. Physical meaning of a clay fraction greater than 1 is that there exists only clay for that particle size. Interest is in the bulk aerosol mineral fractions, next the soil and aerosol clay and silt fractions are combined to produce a total aerosol mineral fractional abundance. First, we determine the fraction of total dust aerosol from the clay and silt sizes by summation (over equivalent diameter bin widths) of fE_{clay} and fE_{silt} averaged over the volume size distribution ($\frac{dV_d}{dlnD_d}$) such that,

$$\frac{dV_d}{dlnD_d} = \frac{D_d}{c_V}[1 + erf\frac{ln(D_{clay}/\bar{D}_s)}{\sqrt{2}ln(\sigma_s)}]exp[-(\frac{D_d}{\lambda})^3]$$

$$\frac{dV_d}{dD_d} = \frac{dV_d}{dlnD_d}/D_d$$

$$fE_{c,aerosol} = \frac{\sum fE_{clay} * dV_d/dD_d}{\sum dV_d/dD_d}$$

$$fE_{s,aerosol} = \frac{\sum fE_{silt} * dV_d/dD_d}{\sum dV_d/dD_d}$$

where V_d is the normalized volume of size D_d dust aerosols, c_V is a normalization constant ($c_V = 12.62\mu$m), and λ is the side crack propagation length obtained from measured fragmentation of brittle materials ($\lambda = 12 \pm 1\mu$m) (Kok, 2011). $fE_{c,aerosol}$ and $fE_{s,aerosol}$ are then combined with the individual soil clay and silt fractions producing the aerosol fraction of each mineral ($fE_{aerosol,i}$).

$$fE_{aerosol,i} = fE_{c,aerosol} * fE_{c,i} + fE_{s,aerosol} * fE_{s,i}$$

We recognize the assumptions made in our derivations of $fE_{aerosol,i}$ generate uncertainties. Specifically, reliance on surface mineral fractions to partition the dust aerosol fraction is uncertain due to temporal and spatial variability influences on the size distribution aloft (Mahowald

et al., 2014). Despite how the particle sizes may change from emission source to boundary layer entrained particles, the AVIRIS/EMIT soil composition products are a critical step in understanding post emission direct dust aerosol effects, notwithstanding time evolution. Having derived the aerosol mineral fractions, a bulk dust aerosol refractive index can now be calculated.

1.2 Derivation of a Bulk Aerosol Refractive Index

Aerosol population shape, morphology, and overall heterogeneity is described by the mixing state (Riemer et al., 2019). Fully internally mixed aerosols contain equivalent proportion of each species per particle. A fully externally mixed aerosol population is one in which each particle is composed of a single species (Stevens and Dastoor, 2019). In a more rigorous sense, populations can be treated as an internal or external mixture, where the former is a material, or particle in our case, composed of a host matrix and a number of inclusions (n) and the latter is a distribution of particles in a confined spherical volume with constant density inside the sphere (Markel, 2016). We first utilize the matrix/inclusion formulation to derive an internally mixed dust aerosol population following the Maxwell-Garnett (MG) formula for heterogeneous mixtures (Niklasson et al., 1981; Scanza et al., 2015). In this section, we apply the ubiquitous assumption that particles are spheres as was invoked originally by Maxwell-Garnett in 1904. The bulk CRI can also be modeled following the Bruggeman mixing method and standard volume mixing rule, which are additionally performed for the purpose of comparison. The Bruggeman method treats all components of the particle medium symmetrically, in that, no inclusion is chosen as the host material (Markel, 2016). Furthermore, assignment of a bulk internal mixture to our single mode distribution at emission is in agreement with the Community Atmosphere Model version 5.0 (CAM 5) Modal Aerosol Module (MAM) which assumes an internal mixing state for individual aerosol modes (Liu et al., 2012).

Complex refractive indices (N) for each AVIRIS/EMIT mineral are sourced from multiple experimental studies that supply values for an uncommon range of wavelengths (Scanza et al.,

2015). A common shortwave (0.1 - 3μm, 0.01μm resolution) and longwave (3.1 - 20 μm, 0.1 μm resolution) set of wavelengths are utilized in a linear interpolation of each mineral N (Figure 1.2). With individual mineral N, for a common wavelength spectrum and resolution, we next calculate the complex dielectric constant (ε) for the individual minerals,

$$\varepsilon = N^2$$

or in terms of the real and imaginary components,

$$\varepsilon = (n + ki)^2$$

where n is the real part of N, k is the imaginary part of N, and i is the imaginary unit.

For particles composed of a heterogeneous mixture of inclusions, the matrix is one component determined by a much larger volume fraction. The matrix dielectric constant ε_m is parameterized differently in the MG formula than the symmetrically parameterized dielectric constants of the inclusions (ε_n, n = 1,2,3,...N). The MG formula used for computing the effective dielectric constant of a multi-component mixture is

$$\varepsilon_{MG} = \varepsilon_m[1 + \frac{3f_n(\frac{\varepsilon_n - \varepsilon_m}{\varepsilon_n + 2\varepsilon_m})}{1 - f_n(\frac{\varepsilon_n - \varepsilon_m}{\varepsilon_n + 2\varepsilon_m})}]$$

and for the AVIRIS/EMIT 11 mineral bulk mixture,

$$\varepsilon_{MG} = \varepsilon_m[1 + \frac{3\sum_{n=1}^{n=11} f_n(\frac{\varepsilon_n - \varepsilon_m}{\varepsilon_n + 2\varepsilon_m})}{1 - \sum_{n=1}^{n=11} f_n(\frac{\varepsilon_n - \varepsilon_m}{\varepsilon_n + 2\varepsilon_m})}]$$

where ε_{MG} is the MG calculated mixture dielectric constant and f_n ($fE_{aerosol,i}$ in the dust particle computation) is the volume fraction of the n-th component. If both matrix and inclusions were to be treated symmetrically, under the condition of near equivalent inclusion volume fractions, the Bruggermen mixing formula can be applied. The equation describing the Bruggemen method of

the mixture ε_{BG} is of the form:

$$\sum_{n=1}^{n=N} f_n \frac{\varepsilon_n - \varepsilon_{BG}}{\varepsilon_n + 2\varepsilon_{BG}} = 0$$

where the sum of the inclusion volume fractions is unity. Comparison with volume averaging to obtain the mixture N has been performed, but subsequent calculation of optical properties has been found to deviate significantly from experimental values (Li and Sokolik, 2018). However, for what soil type and mineral composition circumstance to use each method to retrieve N is

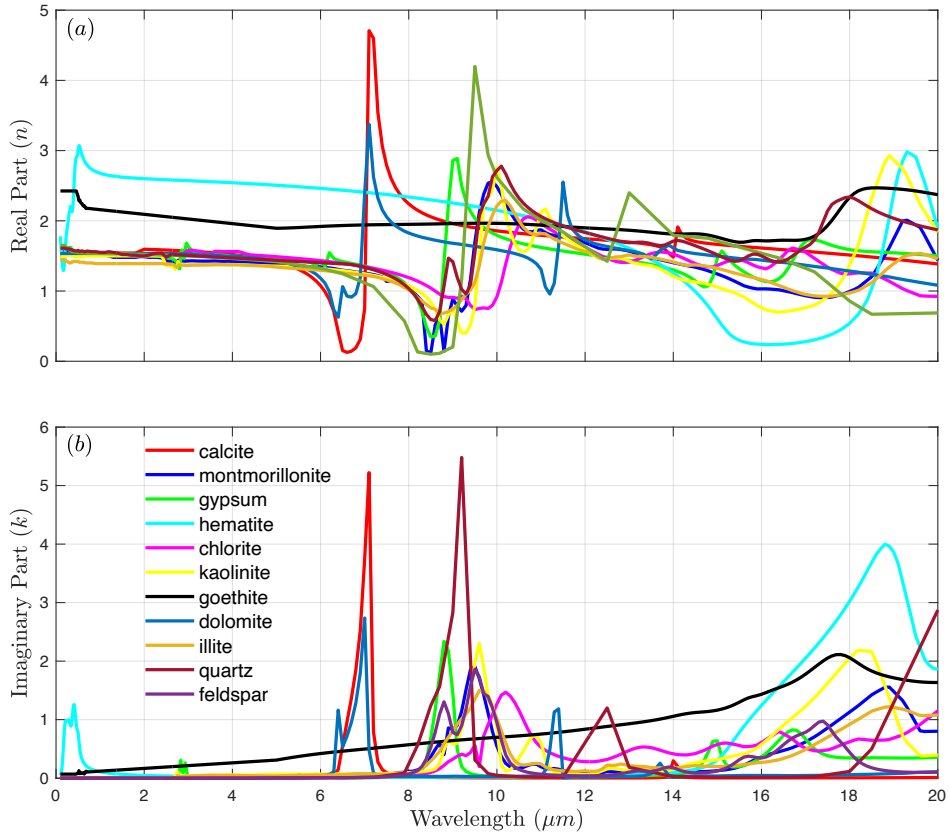

Figure 1.2. Complex index of refraction separated into the real (a) and imaginary (b) parts for the 11 mineral species. Included are 9 AVIRIS/EMIT minerals with the addition of quartz and feldspar whose soil fractions are not mapped. Hematite and goethite are the dominant absorbing species in the solar band. In the imaginary part (k) of calcite, quartz, and feldspar there exists a strong absorption signature near wavelenghts 7 and 9 μm, and the contribution of hematite becomes dominant at wavelengths > 14 μm.

without consensus in the literature. Therefore, the MG rule is favored in application based on the distinguishable matrix/inclusion asymmetry in the derived volume fractions of the mineral dust aerosol, but the Bruggeman and volume mixing methods are applied as well. The bulk aerosol complex refractive index (N_m) is then calculated following the relationship between N and ε

$$N_m = \sqrt{\varepsilon_m}$$

such that N_m is proposed to represent the post-emission overlying aerosol population. The resulting refractive index has an imaginary part that is responsible for the absorption properties of the airborne dust. N_m is then used, in part, to calculate the aerosol optical properties for input into a radiative transfer model (RTM).

1.3 Optical Modeling of Mineral Dust

Computation of aerosol radiative effects in RTMs requires description of their specific optical properties. Most methods of generating these optical properties employ online calculators or other complex algorithms based on Mie Theory, where aerosol particle shapes are spherical. Mie Theory states that the single-scatter of an aerosol depends on the distribution of different sizes with particles of diameter near the incident radiation wavelength effective in scattering radiation (Mie, 1908). The usefulness of Mie Theory is the simplicity of the sphere assumption that is representative of some aerosols types, such as water-soluble aerosols. Particle size and wavelength dependent refractive index collusion produces the aerosol optical properties (Tegen and Lacis, 1996). Under low relative humidity and actual atmospheric conditions Mie Theory does not represent all realistic particle shapes. Limited observations of dust particle shapes, which are imaged with electron microscopy techniques, add additional complexity to modeling particle asphericity. Modeled optical properties of mineral aerosols under the spherical particle assumption have been shown to differ when compared to properties derived from irregular particles, particularly for the phase function in the shortwave (Koepke and Hess,

1988; Nousiainen, 2009; Koepke et al., 2015). The implication of these discrepancies between models is the potential error in the direction of scattering and, moreover, changing the DRE.

Interest in a more realistic representation of particle shape was cause for use of the Texas A&M University dust 2020 (TAMUdust2020) optical properties database version 1.1.0 (Saito et al., 2021). Here, we input the derived spectrally dependent bulk complex index of refraction, aerosol particle sizes, and degree of particle sphericity into the user-defined aerosol optical property model. The TAMUdust2020 database consists of 20 irregular hexahedral particle shape models and light scattering computation. Dust aerosol shape irregularity adds an additional computation to optical property modeling and greatly increases possible particle shape variability (Cattrall et al., 2005). The TAMUdust2020 particle shape model utilizes an ensemble of irregular hexahedral particles to model aerosol shape variability that is weighted by the specified degree of sphericity. A dust particle representative value of 0.7 is used for particle sphericity. For aerosol scattering, the size of the particles is the most important factor. The TAMUdust2020 code applies "state-of-the-art" methods for the radiation scattering computation based on the size appropriate scattering regime (Rayleigh, Mie, or geometric optics). Single scatter properties from the ensemble model, in the short and longwave, are formatted using a kernel technique. Final output upon running the database code includes, for each wavelength and particle diameter, the particle volume (μm^3), projected area (μm^2), extinction efficiency (Q_{ext}), single-scattering albedo (ω or SSA), asymmetry factor (g), and the phase matrix ($\mathbf{P}$) of the randomly oriented particles.

The spectrally dependent dust extinction coefficient (B_{ext}), single-scattering albedo (ω), and asymmetry parameter (g) are calculated from the TAMUdust2020 output by

$$\beta_{ext}(\lambda) = \int_{D_{min}}^{D_{max}} A(D) Q_{ext}(\lambda, D) n(D)\, dD$$

$$\omega(\lambda) = \frac{\int_{D_{min}}^{D_{max}} A(D) Q_{sca}(\lambda, D) n(D)\, dD}{\int_{D_{min}}^{D_{max}} A(D) Q_{ext}(\lambda, D) n(D)\, dD}$$

$$g(\lambda) = \frac{\int_{D_{min}}^{D_{max}} A(D) Q_{sca}(\lambda, D) g(\lambda, D) n(D)\, dD}{\int_{D_{min}}^{D_{max}} A(D) Q_{sca}(\lambda, D) n(D)\, dD}$$

where the limits of integration are over the dust particle size range and A is the particle projected area. These optical properties determine dust/radiation interaction that is the basis for their direct radiative forcing. We model these interactions following the methods in the next section.

1.4 Aerosol-Radiation Modeling

To quantify the direct radiative effect (DRE) of mineral dust we use the Rapid Radiative Transfer Model (RRTM) (Mlawer et al., 1997). The model output includes fluxes and heating rates throughout the vertically layered atmosphere. RRTM implements a correlated-k approach for the radiative transfer calculation with k-distributions from line-by-line radiative transfer (LBLRTM) code. Multiple scattering is solved via the Discrete Ordinates Radiative Transfer (DISORT) algorithm for both the shortwave and longwave model spectral bands, 0.2 to 12μm and 3.1 to 1000 μm respectively (Table 1.2). Extinction in RRTM is available as a manually input file that contains the relevant optical properties for each aerosol (and/or cloud type in the LW). RRTM input files include a user-specified number of atmospheric layers with pre-defined or manually input vertical layer meteorology. The required parameters to model extinction for each individual aerosol containing layer are the spectrally dependent aerosol optical depth (AOD or τ), single scatter albedo (SSA), and asymmetry parameter (g). These parameters must be defined for each of the spectral bands in RRTM. Spectral variability of AOD is typically modeled following the Angstrom Law

$$\tau(\lambda) = \beta \lambda^{-\alpha}$$

Where λ is the wavelength, β is the AOD at a reference wavelength (i.e, 1 μm), and α is the Angstrom exponent (Ångström, 1964). We utilize the Angstrom expression in deriving a source-scaled set of τ values.

In this study, we model dust emission for each of the 3 origin soil variants and retrieve

Table 1.2. RRTM band number and corresponding λs (in μm) for the shortwave (a) and longwave (b) components. λ_{max}, λ_{min}, and $\bar{\lambda}$ are the maximum, minimum, and mean of each band range.

[a]

Band	1	2	3	4	5	6	7	8	9	10	11	12	13	14
λ_{max}	3.846	3.077	2.500	2.151	1.942	1.626	1.299	1.242	0.778	0.625	0.442	0.345	0.263	12.19
λ_{min}	3.077	2.500	2.151	1.942	1.626	1.299	1.242	0.778	0.625	0.442	0.345	0.263	0.200	3.846
$\overline{\lambda}$	3.462	2.788	2.325	2.046	1.784	1.462	1.270	1.01	0.702	0.533	0.393	0.304	0.232	8.021

[b]

Band	1	2	3	4	5	6	7	8	9	10	11	12	13	14	15	16
λ_{max}	1000	29	20	16	14	12	10	9.259	8.475	7.194	6.757	5.556	4.808	4.444	4.202	3.846
λ_{min}	29	20	16	14	12	10	9.259	8.475	7.194	6.757	5.556	4.808	4.444	4.202	3.846	3.077
$\overline{\lambda}$	514.5	24.5	18	15	13	11	9.629	8.867	7.834	6.976	6.156	5.182	4.626	4.323	4.024	3.462

the corresponding optical properties based on theoretical emission. Before running the model with the derived optical properties, the AOD is scaled to observations to increase the models ability to reproduce the direct effect of dust on the vertical layer fluxes and heating rates. Regional aerosol datasets of ground observations can be accessed from NASA's AERosol RObotic NETwork (AERONET; Holben et al., 1998) including aerosol optical depth records over multiple wavelengths. We retrieve observed AOD (τ= 0.3) at 0.5 μm (due to the relevance as a primary wavelength for consistent data retrieval and RT comparison) that is representative of dust storms around the Salton Sea AERONET site to scale modeled AOD values. The spectral variability of the emitted dust is described following the band version of the Angstrom law (Gueymard, 2001; Ruiz-Arias et al., 2014) such that

$$\tau(\lambda) = \tau_{0.5}(\frac{\lambda}{0.5})^{-\alpha_i}$$

with $\tau(\lambda)$ representing optical depth over each band and α_i is the Angstrom exponent corresponding to each band. Band averaged *SSA* and *g* are calculated via numerical averaging . The optical properties are then recorded for each aerosol containing layer in the RRTM aerosol file.

Prior to quantifying the radiation fluxes, we performed a control run for an atmosphere with no dust aerosol. We then ran 36 total simulations: rrtm runs for the 3 AVRIS/EMIT aerosol

type, 3 mixing types, and 2 unique quartz/feldspar treatments; all with the representative AOD value used to scale the band averaged τ for 18 unique aerosol inputs in each of the SW and LW domains. Radiosonde data retrieved during a dust storm in the Salton Sea region parameterized the meteorology for the RRTM runs. Specification for the input RRTM atmosphere profile includes pressure, temperature, and relative humidity. Absorbing molecular species are set to default values for the mid-latitude summer model atmosphere. Simulations were chosen to occur on the first Julian day of the year (Day = 0) and for the 60°solar zenith angle. Other potential user-specified parameterizations in RRTM remained the default value from the mid-latitude summer atmosphere.

The direct radiative effect (DRE) of an aerosol species is defined as the change in the radiation balance of the atmosphere/Earth by the extinction, via scattering and absorption, of short and longwave radiation. Common convention for quantifying the DRE of an aerosol is to define the surface (SFC), atmosphere (ATM), and the top-of-atmosphere (TOA) flux changes. We calculate the SFC, ATM, and TOA flux change by comparing the RRTM output of the dust and control runs. The radiative forcing (RF) is the change in the net flux or difference of the incoming (downward) and outgoing (upward) fluxes:

$$\Delta F = (F_{dust,down} - F_{ctrl,down}) - (F_{dust,up} - F_{ctrl,up})$$

where $\Delta F(W/m^2)$ is the net radiation and F_{dust} and F_{ctrl} are the irradiance values from including and excluding the aerosol perturbation. The RF at the SFC and TOA are individually calculated directly from the previous equation designated ΔF_{SFC} and ΔF_{TOA} . The RF of dust in the atmosphere ATM is the difference between the TOA and SFC where the TOA is defined as:

$$\Delta F_{TOA} = \Delta F_{SFC} + \Delta F_{ATM}$$

therefore,

$$\Delta F_{ATM} = \Delta F_{TOA} - \Delta F_{SFC}$$

The sign and magnitude of ΔF at each level represents the dust DRE with potential warming (positive value) or cooling (negative value) depending on the impact of the dust in conjunction with other environmental factors (Tegen and Lacis, 1996; Mahowald et al., 2014).

Chapter 2

Results and Discussion

2.1 Bulk Refractive Index

Mineral composition data for the three regions of interest do not include the mass fractions of quartz and feldspar; both large constituents of the source soils (Table 1.1). As stated, the mineral tables are modified to include a quartz and feldpar fraction to account for their radiative effects in the overlying atmosphere. We chose quartz as the parent material in the Maxwell-Garnett mixing procedure due to the minerals large size compared to the other inclusions. Consequently, the dominant minerals in the dust aerosol mass fractions (>85%) sourced from the clark lake, exposed playa, and west desert regions are quartz and feldspar. Resulting values of a bulk refractive index for each dust emitting region of interest reveal both agreement and large areas of variability across the spectrum (Figure 2.1). The real part (n) of the refractve index is responsible for particle reflection and refraction. In the SW to near IR (0.1 - 6 μm) and 14 to 16 μm there is similar spectral dependence for n. Variability between the three mixing methods arises in the 7 to 13 μm region and $> 16\mu$m regions, where the effect of choosing a host material in the MG formulation is revealed. The differences between the MG method versus the Bruggemen and volume methods are dominated by the MG quartz influence. In the far longwave region of our calculations ($> 18\mu$m) the smallest values are associated with the volume mixing method and increasing values for the Bruggeman method, and values nearly twice as large for the quartz dominated MG result.

The imaginary part (k) has similar variability as the real part. Small aerosol mineral fractions for hematite and goethite lead to a noticeable signal in the solar region of the spectrum until, where they dominate with large absorption peaks (Di Biagio et al., 2019. There exists a strong absorption signature near wavelengths 7 to 9 μm, the quartz and feldspar regions. Within this wavelength range, results of the MG and Bruggeman method are smaller than volume mixing for all three emission regions, with the largest difference in the west desert where the Bruggeman peak is twice as large as the MG peak. All three regions lack the absorption peak at 13μm in the MG output that is present for the Bruggeman and volume mixing results.

An evident difference in longwave absorption is the decayed hematite signal for the MG results starting at 16 μm. MG values for the Clark Lake region slightly increase with wavelength

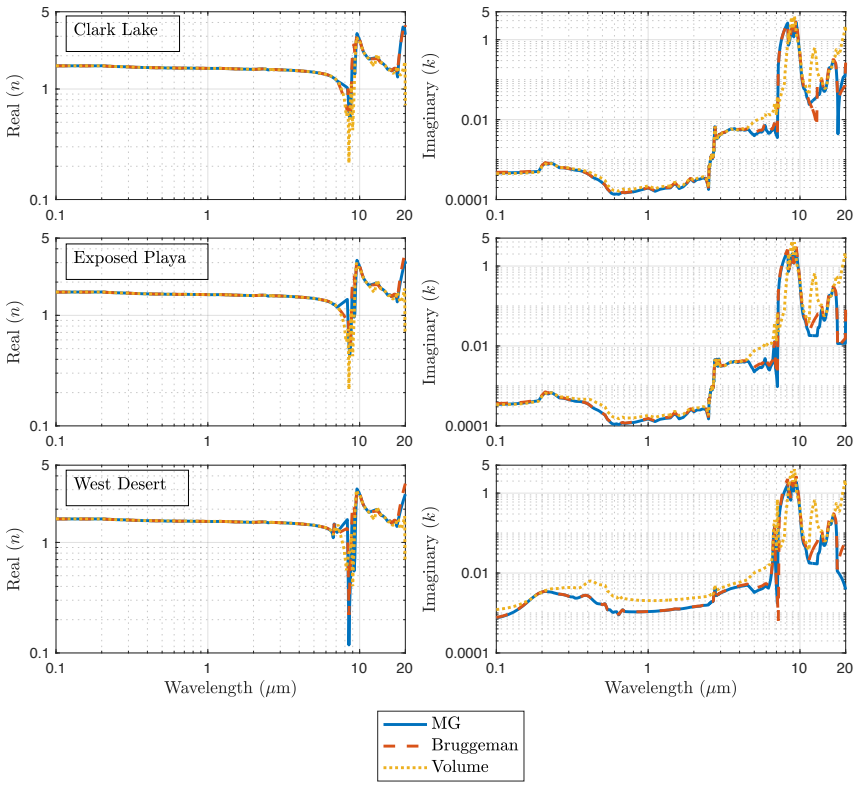

Figure 2.1. Real (n) and Imaginary (k) parts of the complex refractive indices for the three emission regions and three mixing methods. The solid, dashed, and dotted lines indicate the output using the Maxwell-Garnett (MG), Bruggeman, and volume mixing methods.

due to the larger contributions of subsidiary mineral inclusions, namely illite which is an order of magnitude larger than the other regions. In contrast, the contribution of hematite becomes dominant at wavelengths > 16 μm for the Bruggeman and, most obviously, the volume mixing results. The mixing methods CRI trends tend to agree, with the largest departures seen by the volume mixing method. In the next section, presented optical properties reveal these refractive index trends are indicative of the extinction impacts of modeled airborne dust for the emission regions.

2.2 Dust Optical Properties

We compute the dust bulk optical properties for the three emission regions and three mixing methods. The properties of interest are the extinction efficiency (Q_{ext}), single scatter albedo (*SSA*) and asymmetry parameter (g) for use in the radiative transfer model, RRTM. The resulting output from applying an ensemble of irregular shaped particles via the TAMUdust2020 database show good agreement with the absorption expected from the refractive index spectral values. Figure 2.1 presents the dust size integrated, spectrally dependent optical properties for the Clark Lake (CL), Exposed Playa (EP), and West Desert (WD). Shortwave extinction is similar for all three mixing methods and the individual dust types. A steep decrease follows with minimum values < 1.0 between 7 (MG) and 8 (Bruggeman; volume) μm. The extinction efficiency values then reach a maximum of 2.40, 2.35, and 2.28 at 8-9 μm before decreasing with wavelength. At 17 μm the MG values fall to the spectral extinction minimum while Bruggeman and volume rise before all increase to the end of the modeled spectrum.

The *SSA* and asymmetry parameter (g) share the position and frequency of variability with the extinction profile. In the shortwave, *SSA* values increase with wavelength. Similarly, an analysis of regional and global dust CRI and *SSA* variability via a laboratory simulation chamber study by DiBiagio et al. (2019) found increasing *SSA* in the shortwave (0.37 to 0.9 μm) for North American dust (R = 0.99; 0.99; 0.97)Di Biagio et al., 2019. WD iron oxide mineral fractions

are larger than those of CL/EP. The consequence of varying iron oxides is evident in the smaller WD *SSA* (0.1 - 1.2 μm). To note are the differences in these parameters between each mixing method of the emission regions. *SSA* and *g* values diverge in all three plots at the 11 - 14 μm and 16 - 20 μm regions of the spectrum. MG *SSA* values can be larger than BG and VM by 0.5 at these wavelengths. The MG mixing method lends more representation of the chosen parent material in the *SSA* features. Recall the mineral CRI values; in the imaginary part there exists a quartz signal that ends abruptly near 12μm. Larger *SSA* values in the MG method are in tern influenced by the large quartz fraction. Alternatively, the BG and VM methods support a more equivalent mineral influence. Another interesting finding is the infrared feature after 16 μm. Differences within each region are explained by the lack of an absorption peak in the imaginary part of the MG CRI that is present for the BG and VM. Once again, the effect of a large quartz fraction is revealed. In regard to the individual emission regions, CL and, to a lesser extent, EP fractions of other constituent minerals are much greater than those of the WD. Despite quartz being the dominant mineral in the MG method, larger fractions of illite and montmorillionite (key absorbing species in the longwave) are illustrated by the differences in regional MG *SSA*.

The positive values of *g* indicate all three dust types preferentially scatter into the forward hemisphere. Variability in the asymmetry parameter induced by the choice of mixing state are similar to those found for SSA, but less in magnitude. Changes in *g* with wavelength is primarily attributable to the change in the complex refractive index (Curci et al., 2015). For the different mixing methods, larger *SSA* values are associated with smaller *g* values, and vice versa.

We convert Q_{ext} values to extinction coefficients (β_{ext}) before integrating over the height of the aerosol layer for a measure of τ. Band averaged ($\bar{\lambda}$) AOD values are scaled to the 0.5 μm dust representative AOD value (τ = 0.3) for the radiation model input aerosol layer properties. *SSA* and *g* are averaged over each band for use in aerosol-radiation modeling by RRTM.

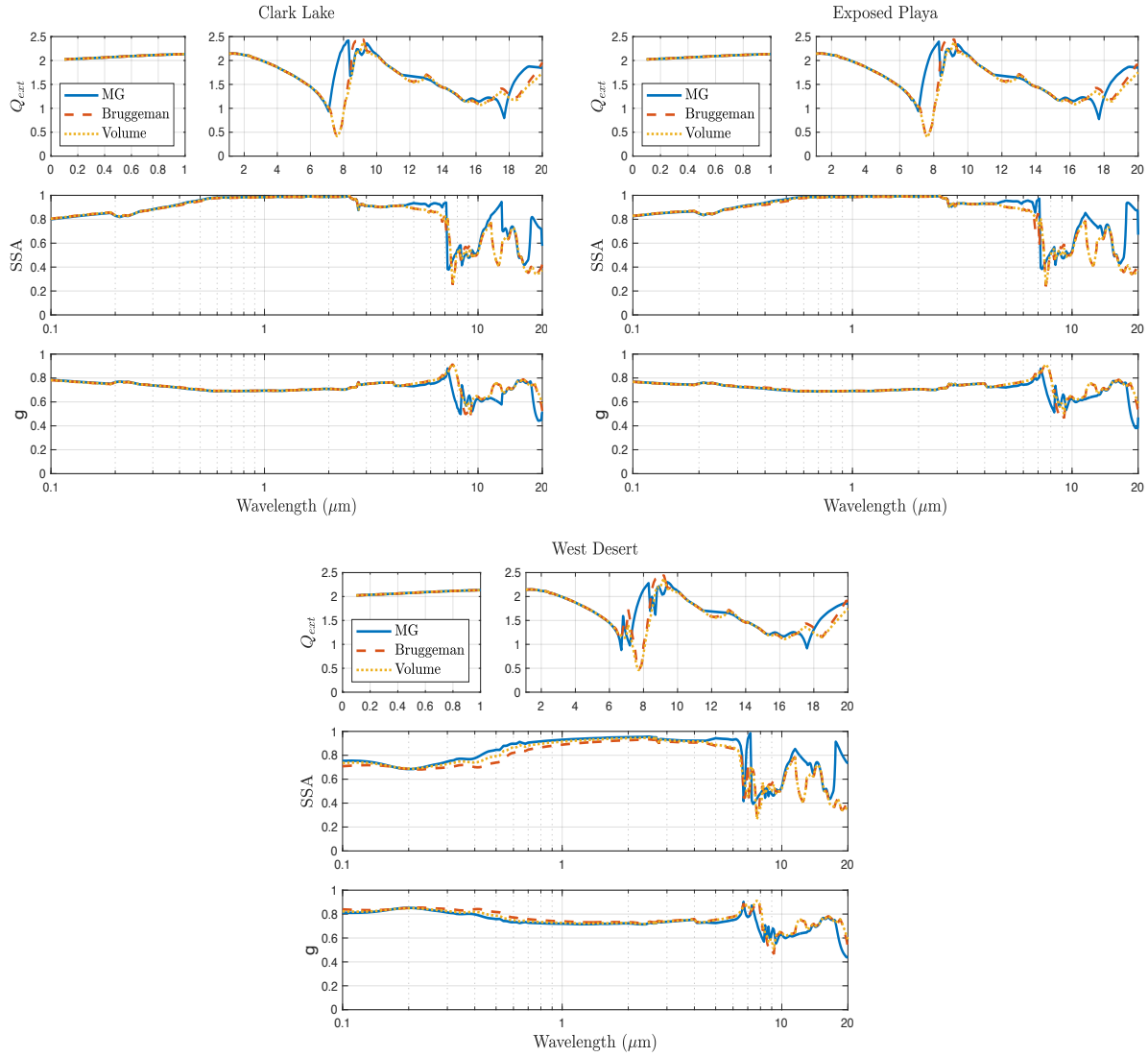

Figure 2.2. Bulk optical properties of the three source regions. Extinction efficiency (Q_{ext}), single scatter albedo (SSA), and asymmetry parameter (g) are included. The solid, dashed, and dotted lines indicate the output using the Maxwell-Garnett (MG), Bruggeman, and volume mixing methods.

2.3 Dust Direct Radiative Effect

Simulations in RRTM are for the entire vertical column, but dust is present only in the first two layers (1 km) in an e-folding vertical distribution (layer 1 (1003 to 946mb) - 66% of AOD, layer 2 (946 to 891mb) - 33% of AOD). Fluxes (Wm^{-2}) and heating rates (Kd^{-1}) for the RRTM runs are displayed in Figure 2.3 with subplots for the control atmosphere run and each emission region. For the TOA and surface for closer examination. The downwelling shortwave shows a similar trend with smaller flux values at the surface for the west desert. Both upwelling and downwelling longwave fluxes are similar for all three emission regions, potentially a consequence of the lack of modeled longwave scattering. The net SW flux has a larger rate of change from the surface to top of dust layer for the west desert region than the other two, a consequence of mineral abundances. Heating rates have similar profiles between the three regions. The WD dust has the largest near surface warming. All three emission regions show net surface cooling. Overall, all three emission regions fluxes indicates a large dust influence on the transmission of shortwave radiation.

The direct radiative effect (DRE) of dust is unique to source soil and environmental conditions where surface properties, particle size distribution, and aerosol species composition contribute to the magnitude and sign of the DRE (Balkanski et al., 2007; Kok et al., 2017). We focus on soil source mineralogy to assess variable dust composition in our analysis of the DRE. By segregating the soil emission regions we are able to compare how source specific bulk dust can affect the solar and infrared fluxes. With these fluxes we are able to determine the radiative forcing of the dusty layer as the difference between the control atmosphere and dusty scenarios. Figure 2.4 is a bar plot of the shortwave (SW), longwave(LW), and net surface, atmosphere, and TOA DRE for the three emission regions. Bar plots extend to the mean values for the SW, LW, and net at each atmospheric level (Table A.2). The mean of the 6 DRE values for each emission region were calculated because the different mineral treatment/mixing method combinations varied by $< 10\%$, except for the SW forcing in the ATM and TOA for the WD.

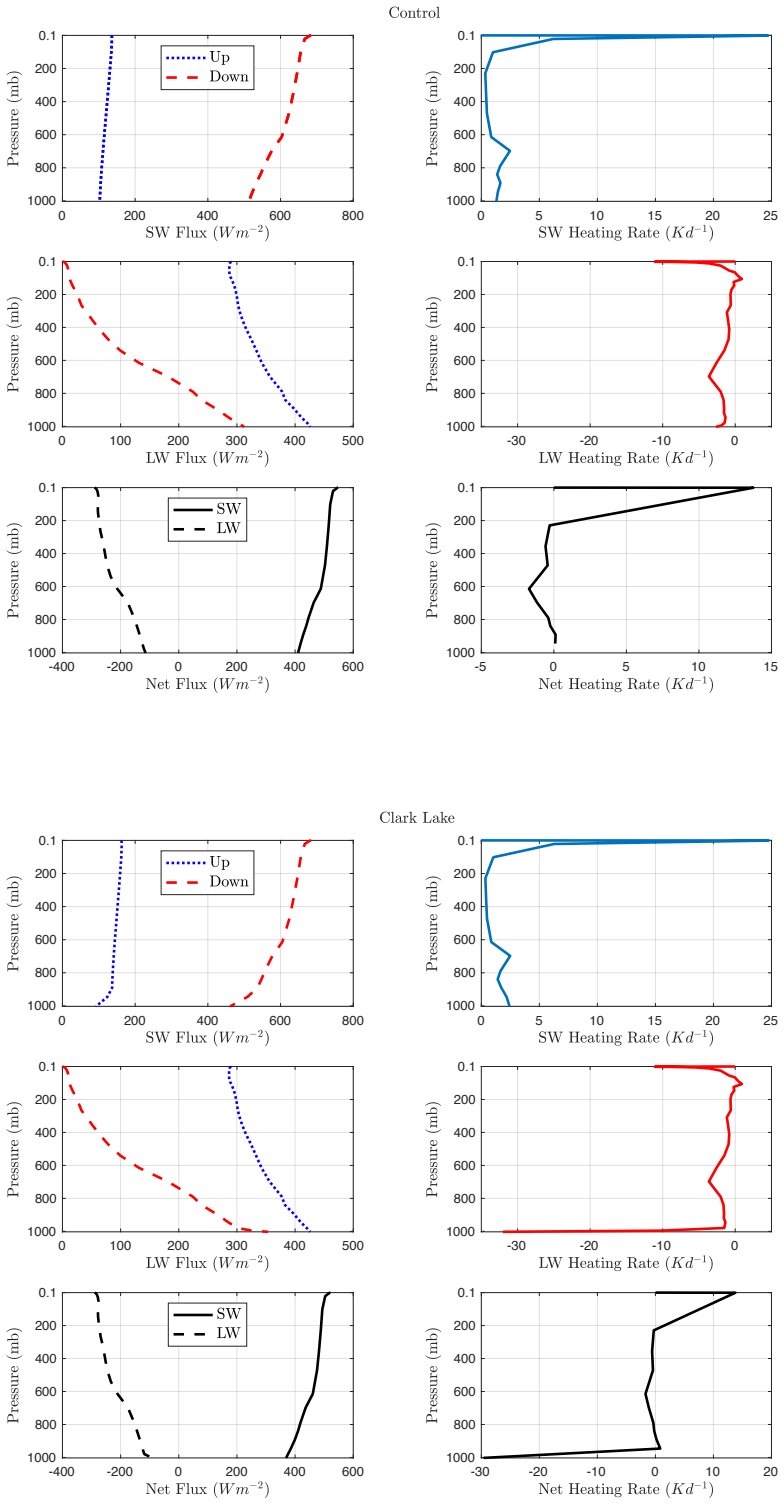

Figure 2.3. Spectrally integrated up, down, net fluxes (Wm^{-2}), and heating rates (Kd^{-1}) for the shortwave (0.2 to 3.0μm) and longwave bands (3.1 to 1000 μm). Shown is the control sky and suspended dust atmosphere for the three emission regions at an aerosol optical depth $\tau = 0.3$.

Figure 2.3. Continued

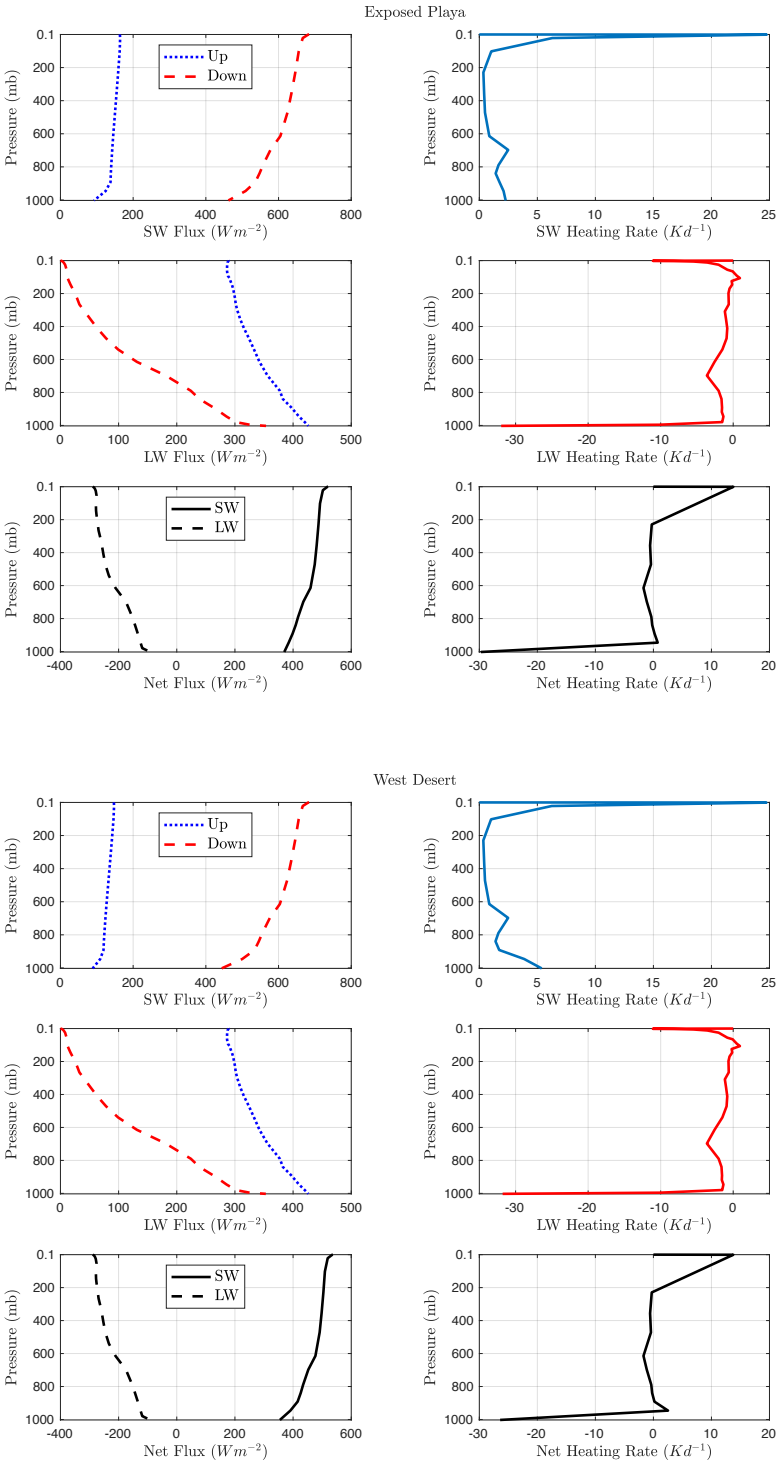

For all three emission regions, in the infrared band, the aerosol layer at the surface is absorbing and emitting energy, causing a warming effect. This relationship between the sign of the radiative forcing and temperature change occurs at each atmospheric layer (i.e., positive is warming; negative is cooling). The radiative forcing in the LW is markedly similar for each dust type. SSA values are consistent across the LW spectrum with most of the divergence seen between mixing methods within the individual regions. Radiation in the solar band is preferentially scattered by the aerosol layer at the surface, causing a cooling effect for the three dust types. While the CL and EP mean RF values differ by hundredths of a percent, the RF of the WD dust is more negative ($\Delta = DRE$ 19.3 Wm^{-2}). The surface discrepancy between the CL/EP and WD dust SW RF is a result of larger WD hematite and goethite soil mineral fractions. Downwelling SW radiation is absorbed at the top of the dust layer (positive SW ATM DRE), decreasing transmission to the surface.

Out of the 11 mineral species, hematite and goethite dominate the imaginary part in the solar region of the spectrum. Maximum absorption by hematite is greater than a value of 1.0 at wavelengths in the visible region (0.2 - 0.6μm) before decaying until the mid-infrared. A constant value of 0.07 at $\lambda < 0.46\mu$m is used for goethite, a consequence of the linear interpolation to create a spectrally complete set of refractive indices. Goethite reaches a maximum value of 0.13 in the visible. Although goethite is the second strongest absorbing species in the shortwave, hematite is substantially larger before 1 μm, from here goethite increases linearly to the mid-infrared. CL/WD and EP/WD percent difference of the hematite and goethite fractions are 96.47%/94.4% and 98.3%/96.5% (Table 1.1). Comparison of the individual RRTM band output reveal the WD surface SW fluxes in the band range 0.44 to 1.24 μm are more negative (-2.447 to -8.77 Wm^{-2}) than the CL/EP values. While all three dust types have a negative (cooling) net radiative forcing at the surface, WD dust is most negative.

The radiative forcing at the TOA is negative ($\sim$ -26.3/-26.96 Wm^{-2}) for the CL/EP dust and more positive (-5.94Wm^{-2}) for WD dust in the solar band. WD TOA fluxes are larger (2.88 to 9.0 Wm^{-2}) than the CL/EP in the previously mentioned SW band range. All three regions

have a small mean radiative forcing ($0.45 \mathrm{Wm}^{-2}$) in the longwave spectrum. Therefore, the net radiative forcing is negative for all three regions, but largest for the WD. The overall magnitude of CL/EP dust is significantly ($> 400\%$) greater than the WD dust. TOA DRE differences between the dust types are attributed to the interactions within the atmosphere. As was the case at the surface, the LW radiative forcing for the three dust types are similar with 0.2 Wm^{-2} separating the CL/EP and WD. The SW radiative forcing of the WD is over 4 times that of the other two dust types. The aformentioned greater hematite and goethite mineral fractions of WD soil is linked to decreased *SSA* in the SW which entails greater absorption of incoming SW radiation. As a result the sign of the TOA net DRE are the same for the WD and CL/EP dust types, but the WD is warmer. These resulting values highlight the distinct radiative effect of modeled mineral composition as a function of soil source. Moreover, from the greater cooling (warming) effect of the CL/EP (WD) dust types we can infer that the static stability of the atmosphere is decreased (increased) when these dust types are the predominate aerosol by mass.

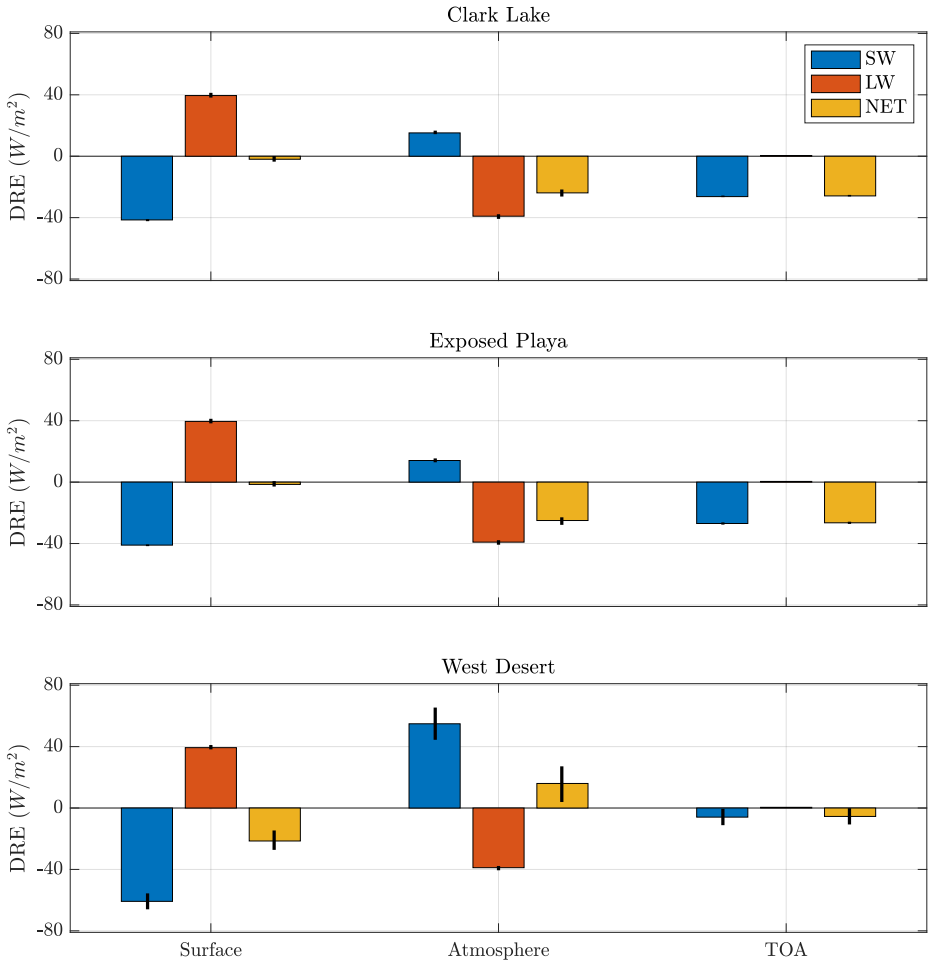

Figure 2.4. DRE (Wm^{-2}) of dust aerosol sourced from the Clark Lake, Exposed Playa, and West Desert. Shown is the surface, atmosphere, and TOA values with SW (blue), longwave (red), and net (yellow) radiative forcings calculated for the dust representative AOD ($\tau = 0.3$).

2.4 Model Uncertainty

A number of assumptions are made during each phase of the DRE resulting methodology. The initial choice of soil type is the first assumption made. The soil mineralogy information originally from Claquin et al. (1999) and updated by Journet et al. (2014) enables our resulting clay and silt aerosol fractions. We further modify the soil mineralogy maps to include the missing AVIRIS/EMIT mineral species that encompass the soil composition products. These findings suggest, however, that treatment of the missing quartz and feldspar surface mineral fractions does not significantly impact the resulting DRE. Choice of treatment for hematite and goethite can impact the sign of resulting DRE calculations (See Appendix A). Previous studies exclude the goethtite CRI values by simulating the iron oxides collectively as hematite; finding a positive TOA forcing for mineral dust in these cases (Scanza et al., 2015; Li and Sokolik, 2018). Here, components of absorbing dust are modeled separately as access to goethite CRI values and soil abundance fractions were available. Despite the supplied information, quantifying the *in situ* clay and silt soil fractions in addition to the particle size distribution of the soil would enhance our ability more accurately calculate the DRE. Furthermore, in modeling the irregular shape of the dust we enter into a relatively new domain of deriving dust's single scatter properties, especially starting from soil mineral fraction derived dust CRI values. Use of RRTM is commonplace and validated against highly accurate line-by-line radiative transfer models (LBLRTM), however, the implementation and evaluation of dust properties in the longwave kernal for this study version does not include scattering. These assumptions and results, that are not fully realized, create the necessity for future evaluation of model uncertainty so as to constrain the radiative impact of dust in the local atmosphere.

Chapter 3

Conclusion

The methods and results presented here are an early impact study on future products from NASA's EMIT mission. We aggregate existing and novel methodology to quantify the direct radiative effect of dust from source soil mineralogy. Specific focus on regional AVIRIS flight data enabled the derivation of CRIs for multiple emission locations. Information on arid and semi-arid soil mineralogy from updated soil databases supplemented the surface mineral composition data for a more representative aerosol size distribution. In parallel with recent work, we followed the Maxwell-Garnett mixing rule to produce an internal mixture of the mineral components when defining particle composition. We also calculated the mixing results from the Bruggeman and volume mixing methods for comparison. To model emission, without heavy computational requirements associated with particle transport in general circulation models, we leverage dust emission theory from Kok et al. (2011) and present bulk aerosol properties.

Our calculations of the dust optical properties builds off of continued efforts to model more realistic dust particle shapes. The TAMUdust2020 database employs a number of techniques to produce the single scatter properties of irregular particles. Implementation of the database led to unique results for the three emission regions we modeled. Dust types shared common features in the sw and deviated more obviously in the LW. CRI from MG method has distinct trends that are not shared by the Bruggeman and volume mixing methods. Quartz as the parent material in the MG method masks the effect other mineral signatures in the imaginary

part of the CRI.

The emission region differences are visible in the spectral integrated fluxes and heating rates, but the mixing methods do not produce substantial variation in the results. Importantly, the benefit of the irregular particle model for the optical properties is hindered by the lack of scattering in the RRTM longwave runs. When full extinction is considered (i.e., model multiple scattering in the LW), the RRTM fluxes may change with the impact of the mixing methods revealed.

The local direct radiative effect for the three emission regions and mixing methods at the surface, atmosphere, and TOA was determined following the aforementioned methods. From our simulations the TOA has a net DRE range of -26.5 to -5.59 Wm^{-2} between the emission regions. Comparatively, Li Sokolik (2018) found cooling and warming effects at the surface and in the atmosphere (TOA DRE: -46 Wm^{-2}) using a MG method fitting procedure. Results indicate that the dust types studied here have a smaller TOA cooling effect. The mechanism found to increase TOA forcing in Scanza et al. (2015) was high concentrations of hematite over key global emission regions. Net TOA values presented here agree with these mineralogy driven variations. The DRE at the surface is found to be between -21.48 and -1.49 Wm^{-2}. The west desert has the largest cooling effect of the emission regions at the surface due to higher fractions of iron oxide containing minerals hematite and goethite. Mineral dust has a cooling effect in the atmosphere for CL/EP and a warming effect for the WD (-25.01 to 15.99 Wm^{-2}; the largest range of the atmosphere levels). Longwave scattering may play a critical role in this difference between regional DRE. If the west desert *SSA* peak at 7 μm was realized during the radiative transfer simulations, a decreased surface LW forcing may have ensued that would cool the TOA. These results are sensitive to poorly constrained methods of mineral aerosol derivation and subsequent model simulations.

Analogous simulations and sensitivity tests of the numerous parameters used here is required to better represent mineral dust from the fractional component level to the bulk mixture. The vertical distribution of dust and the temporal changes associated with transport are not

considered here. The modeled DRE results presented in this thesis are the first of its kind for these regional emission sources. Results indicate higher resolution mineral soil composition measurements from EMIT will enable more accurate measurements of regional dust DRE. In effort to determine the viability of the methods and study as a whole more simulations are required. Next steps include a case study of the diurnal cycle of dust storm events surrounding the Salton Sea and comparison with ground based flux measurements at the emission site.

Appendix A

Results and Discussion

Table A.1. Dust instantaneous radiative forcing (Wm^{-2}) calculated for the three emission regions and mixing methods. SW and LW RF for each atmosphere layer are calculated from the RRTM output fluxes. The net value is the sum of the SW and LW forcings. Hematite and goethite are treated separately.

Level	Region	SW	LW	Net
SFC	CL	−41.49 ±0.58	39.52±1.20	−1.97 ±1.44
	EP	−41.04 ±0.47	39.55±1.15	−1.49 ±1.43
	WD	−60.80 ±4.22	39.33±1.10	−21.48 ±5.10
ATM	CL	15.19±1.04	−39.07 ±1.19	−23.88 ±1.77
	EP	14.08±1.03	−39.10 ±1.13	−25.01 ±1.96
	WD	54.87±8.56	−38.87 ±1.09	15.99±9.40
TOA	CL	−26.30 ±0.46	0.45±0.02	−25.85 ±0.46
	EP	−26.96 ±0.58	0.45±0.02	−26.51 ±0.57
	WD	−5.94 ±4.34	0.45±0.01	−5.49 ±4.33

Table A.2. Dust instantaneous radiative forcing (Wm^{-2}) calculated for the three emission regions and mixing methods. SW and LW RF for each atmosphere layer are calculated from the RRTM output fluxes. The net value is the sum of the SW and LW forcings. Hematite and goethite are treated collectively as hematite.

Level	Region	SW	LW	Net
SFC	CL	−43.53 ±1.19	39.52±1.20	−4.01 ±2.09
	EP	−42.73 ±1.30	39.52±1.15	−3.21 ±2.31
	WD	−65.32 ±5.91	39.23±1.02	−26.09 ±6.25
ATM	CL	19.25±2.62	−39.07 ±1.19	−19.82 ±3.44
	EP	17.64±2.84	−39.07 ±1.14	−21.43 ±3.80
	WD	62.89±11.50	−38.78 ±1.01	24.11±11.84
TOA	CL	−24.28 ±1.44	0.45±0.02	−23.83 ±1.43
	EP	−25.10 ±1.55	0.45±0.02	−24.65 ±1.54
	WD	−2.42 ±5.60	0.45±0.01	−1.98 ±5.60

Bibliography

A. Ångström. The parameters of atmospheric turbidity. *Tellus*, 16(1):64–75, 1964.

Y. Balkanski, M. Schulz, T. Claquin, and S. Guibert. Reevaluation of mineral aerosol radiative forcings suggests a better agreement with satellite and aeronet data. *Atmospheric Chemistry and Physics*, 7(1):81–95, 2007.

C. Cattrall, J. Reagan, K. Thome, and O. Dubovik. Variability of aerosol and spectral lidar and backscatter and extinction ratios of key aerosol types derived from selected aerosol robotic network locations. *Journal of Geophysical Research: Atmospheres*, 110(D10), 2005.

T. Claquin, M. Schulz, and Y. Balkanski. Modeling the mineralogy of atmospheric dust sources. *Journal of Geophysical Research: Atmospheres*, 104(D18):22243–22256, 1999.

G. Curci, C. Hogrefe, R. Bianconi, U. Im, A. Balzarini, R. Baró, D. Brunner, R. Forkel, L. Giordano, M. Hirtl, L. Honzak, P. Jimenez-Guerrero, C. Knote, M. Langer, P. Maker, and G. Pirovano. Uncertainties of simulated aerosol optical properties induced by assumptions on aerosol physical and chemical properties: An aqmeii-2 perspective. *Atmospheric Environment*, 115:541–552, 2015.

C. Di Biagio, P. Formenti, Y. Balkanski, L. Caponi, M. Cazaunau, E. Pangui, E. Journet, S. Nowak, M. O. Andreae, K. Kandler, T. Saeed, S. Piketh, D. Seibert, E. Williams, and J.-F. Doussin. Complex refractive indices and single-scattering albedo of global dust aerosols in the shortwave spectrum and relationship to size and iron content. *Atmospheric Chemistry and Physics*, 19(24):15503–15531, 2019.

P. D'Odorico, A. Bhattachan, K. F. Davis, S. Ravi, and C. W. Runyan. Global desertification: drivers and feedbacks. *Advances in water resources*, 51:326–344, 2013.

D. A. Gillette, I. H. Blifford Jr, and D. Fryrear. The influence of wind velocity on the size distributions of aerosols generated by the wind erosion of soils. *Journal of Geophysical Research*, 79(27):4068–4075, 1974.

A. S. Goudie and N. J. Middleton. The changing frequency of dust storms through time. *Climatic change*, 20(3):197–225, 1992.

R. O. Green, N. Mahowald, C. Ung, D. R. Thompson, L. Bator, M. Bennet, M. Bernas, N. Blackway, C. Bradley, J. Cha, P. Clark, R. Clark, D. Cloud, D. Ernesto, E. Ben Dor, R. Duren, and M. Eastwood. The earth surface mineral dust source investigation: An earth science imaging spectroscopy mission. In *2020 IEEE Aerospace Conference*, pages 1–15. IEEE, 2020.

C. A. Gueymard. Parameterized transmittance model for direct beam and circumsolar spectral irradiance. *Solar Energy*, 71(5):325–346, 2001.

B. N. Holben, T. F. Eck, I. a. Slutsker, D. Tanre, J. Buis, A. Setzer, E. Vermote, J. A. Reagan, Y. Kaufman, T. Nakajima, F. Lavenu, I. Jankowiak, and A. Smirnov. Aeronet—a federated instrument network and data archive for aerosol characterization. *Remote sensing of environment*, 66(1):1–16, 1998.

E. Journet, Y. Balkanski, and S. P. Harrison. A new data set of soil mineralogy for dust-cycle modeling. *Atmospheric Chemistry and Physics*, 14(8):3801–3816, 2014.

P. Koepke and M. Hess. Scattering functions of tropospheric aerosols: the effects of nonspherical particles. *Applied Optics*, 27(12):2422–2430, 1988.

P. Koepke, J. Gasteiger, and M. Hess. Optical properties of desert aerosol with non-spherical mineral particles: data incorporated to opac. *Atmospheric Chemistry and Physics*, 15(10): 5947–5956, 2015.

J. F. Kok. A scaling theory for the size distribution of emitted dust aerosols suggests climate models underestimate the size of the global dust cycle. *Proceedings of the National Academy of Sciences*, 108(3):1016–1021, 2011.

J. F. Kok, D. A. Ridley, Q. Zhou, R. L. Miller, C. Zhao, C. L. Heald, D. S. Ward, S. Albani, and K. Haustein. Smaller desert dust cooling effect estimated from analysis of dust size and abundance. *Nature Geoscience*, 10(4):274–278, 2017.

A. N. Kolmogorov. On the logarithmically normal law of distribution of the size of particles under pulverization. In *Dokl. Akad. Nauk SSSR*, volume 31, page 99, 1941.

F. Li, A. Vogelmann, and V. Ramanathan. Saharan dust aerosol radiative forcing measured from space. *Journal of Climate*, 17(13):2558–2571, 2004.

L. Li and I. N. Sokolik. The dust direct radiative impact and its sensitivity to the land surface state and key minerals in the wrf-chem-dumo model: A case study of dust storms in central asia. *Journal of Geophysical Research: Atmospheres*, 123(9):4564–4582, 2018.

X. Liu, R. C. Easter, S. J. Ghan, R. Zaveri, P. Rasch, X. Shi, J.-F. Lamarque, A. Gettelman, H. Morrison, F. Vitt, A. Conley, S. Park, R. Neale, C. Hannay, A. Ekman, P. Hess, and N. Mahowald. Toward a minimal representation of aerosols in climate models: Description

and evaluation in the community atmosphere model cam5. *Geoscientific Model Development*, 5(3):709–739, 2012.

N. Mahowald, S. Albani, J. F. Kok, S. Engelstaeder, R. Scanza, D. S. Ward, and M. G. Flanner. The size distribution of desert dust aerosols and its impact on the earth system. *Aeolian Research*, 15:53–71, 2014.

N. M. Mahowald and L. M. Kiehl. Mineral aerosol and cloud interactions. *Geophysical Research Letters*, 30(9), 2003.

V. A. Markel. Introduction to the maxwell garnett approximation: tutorial. *JOSA A*, 33(7): 1244–1256, 2016.

G. Mie. Beiträge zur optik trüber medien, speziell kolloidaler metallösungen. *Annalen der physik*, 330(3):377–445, 1908.

E. J. Mlawer, S. J. Taubman, P. D. Brown, M. J. Iacono, and S. A. Clough. Radiative transfer for inhomogeneous atmospheres: Rrtm, a validated correlated-k model for the longwave. *Journal of Geophysical Research: Atmospheres*, 102(D14):16663–16682, 1997.

G. Myhre, D. Shindell, F.-M. Bréon, W. Collins, J. Fuglestvedt, J. Huang, D. Koch, J.-F. Lamarque, D. Lee, B. Mendoza, T. Nakajima, A. Robock, G. Stephens, T. Takemura, and H. Zhang. *Anthropogenic and natural radiative forcing*, pages 659–740. Cambridge University Press, Cambridge, UK, 2013. doi: 10.1017/CBO9781107415324.018.

G. A. Niklasson, C. Granqvist, and O. Hunderi. Effective medium models for the optical properties of inhomogeneous materials. *Applied Optics*, 20(1):26–30, 1981.

T. Nousiainen. Optical modeling of mineral dust particles: A review. *Journal of Quantitative Spectroscopy and Radiative Transfer*, 110(14-16):1261–1279, 2009.

N. Riemer, A. Ault, M. West, R. Craig, and J. Curtis. Aerosol mixing state: Measurements, modeling, and impacts. *Reviews of Geophysics*, 57(2):187–249, 2019.

D. Rosenfeld, Y. Rudich, and R. Lahav. Desert dust suppressing precipitation: A possible desertification feedback loop. *Proceedings of the National Academy of Sciences*, 98(11): 5975–5980, 2001.

J. A. Ruiz-Arias, J. Dudhia, and C. A. Gueymard. A simple parameterization of the short-wave aerosol optical properties for surface direct and diffuse irradiances assessment in a numerical weather model. *Geoscientific Model Development*, 7(3):1159–1174, 2014.

M. Saito, P. Yang, J. Ding, and X. Liu. A comprehensive database of the optical properties of irregular aerosol particles for radiative transfer simulations. *Journal of the Atmospheric*

Sciences, 78(7):2089–2111, 2021.

R. Scanza, N. Mahowald, S. Ghan, C. Zender, J. Kok, X. Liu, Y. Zhang, and S. Albani. Modeling dust as component minerals in the community atmosphere model: development of framework and impact on radiative forcing. *Atmospheric Chemistry and Physics*, 15(1):537–561, 2015.

Y. Shao. A model for mineral dust emission. *Journal of Geophysical Research: Atmospheres*, 106(D17):20239–20254, 2001.

R. Stevens and A. Dastoor. A review of the representation of aerosol mixing state in atmospheric models. *Atmosphere*, 10(4):168, 2019.

I. Tegen and A. A. Lacis. Modeling of particle size distribution and its influence on the radiative properties of mineral dust aerosol. *Journal of Geophysical Research: Atmospheres*, 101(D14): 19237–19244, 1996.